

# Statistical Parameter Inference of a 3D Solid Breast Texture Model from Clinical Breast Computerized Tomography Data

Zhijin Li, *Member, IEEE*, Ann-Katherine Carton, Serge Muller and Agnès Desolneux, *Member, IEEE*,

**Abstract**—The abstract goes here.

**Index Terms**—X-ray breast imaging, virtual clinical trials, 3D breast texture model, stochastic geometry, statistical parameter inference.

## I. INTRODUCTION AND MOTIVATION

XXXX [TO BE FINISHED]

THE parameters of our previously proposed 3D solid breast texture model can be classified into two categories:

- 1) The parameters related to the *small scale* breast fibroglandular and inter-glandular adipose tissue. These parameters include the intensity  $\lambda_0$  of the Poisson point process for the Voronoi cell centers and the precision parameter  $\epsilon$  of the voxelization process.
- 2) The parameters related to the distribution and morphology of the *medium scale* breast fibroglandular and inter-glandular adipose tissue. These parameters include the distribution  $\mathbf{P}^s$  of the ellipsoid center point process  $\Phi_s$  and the joint distribution  $\mathbf{P}^\theta$  of  $\theta$ , the random vector related to the shape and orientation of the random ellipsoids.

XXXX [TO BE FINISHED]

## II. PROBLEM FORMULATION

IN this paper, we focus on objective inference of the medium scale model parameters  $\mathbf{P}^s$  and  $\mathbf{P}^\theta$  from segmented clinical bCT data sets. The reason to consider only the medium scale model is mainly due to the relatively low spatial resolution of the clinical bCT data, where the voxel size is typically between 0.2 mm and 0.4 mm. When the intensity parameter  $\lambda_0$  has a relatively large value, the size of the small Voronoi cells may be in the same order of magnitude as the voxel size in the bCT data. Due to this fact, the bCT data may not allow to perform an accurate estimation of the small scale model parameters.

Zhijin Li is with centre de mathématique et leurs applications of Ecole Normale Supérieure de Paris-Saclay, Cachan, 94235 France and General Electric Healthcare France, Buc, 78530, France. E-mail: jonathan.li@ge.com.

Agnès Desolneux is with centre de mathématique et leurs applications of Ecole Normale Supérieure de Paris-Saclay, Cachan, 94235 France.

Ann-Katherine Carton and Serge Muller are with General Electric Healthcare France, Buc, 78530, France.

Manuscript received December, XXXX; revised January XX, XXXX.

We first start by mathematically formulating the inference problem.

### A. The medium scale texture model

We formulated the medium scale texture model as a *marked point process* (MPP)

$$\mathbf{Y} = \{\Phi_s, \theta\},$$

defined on a product space  $Y \subset \mathbb{R}^3 \times \mathbb{R}^6$  [?].

- The ellipsoid center point process  $\Phi_s$  is referred to as the *ground point process*. It is a simple point process with distribution  $\mathbf{P}^s$ .
- The elements of the random vector  $\theta$  are referred to as the *marks*. In our case,  $\theta = (L_a, L_b, L_c, \delta_{\phi_a}, \delta_{\phi_b}, \delta_{\phi_c})$ , where  $L_a, L_b, L_c$  are the half lengths of the principle axes of the ellipsoids and  $\delta_{\phi_x}, \delta_{\phi_y}, \delta_{\phi_z}$  are random tilt angles of the ellipsoid. The marks follow is assumed to follow a distribution  $\mathbf{P}^\theta$ .

### B. The ground truth

A set of sixteen clinical dedicated breast computerized tomography (bCT) reconstructed volumes was collected. The reconstructed volumes are stacks of gray-value coronal slices reconstructed with a filtered back-projection algorithm from projections images acquired using a prototype bCT machine developed at the University of California Davis Medical Center [ref]. The volumes were pre-processed by an automatic 3D segmentation algorithm developed in-house to obtain binary volumes depicting breast fibroglandular and intra-glandular adipose tissue. These binary volumes were used as the input data for the parameter inference.

To limit the inference to the medium scale breast tissue, only volumes of interest (VOI) with size  $3.5 \text{ cm} \times 3.5 \text{ cm} \times 3.5 \text{ cm}$  of the segmented bCT volumes were considered. The VOIs were extracted from the center of the segmented bCT volumes, leaving at least 2 cm distance to the breast skin and the chest-wall, depending on the breast size. The size of the VOIs was chosen small enough so that the fibroglandular tissue distribution does not vary drastically. An example illustrating an input segmented bCT VOI is shown in Figure XXX.

Mathematically, a segmented bCT VOI can be expressed as a binary volume  $\mathcal{D}$ , where

$$\mathcal{D}(x) = \begin{cases} 1 & \text{if voxel } x \text{ represents fibroglandular tissue,} \\ 0 & \text{if voxel } x \text{ represents adipose tissue,} \end{cases} \quad (1)$$

for all  $x \in \Omega \subset \mathbb{Z}^3$ . Here  $\Omega$  represents the 3D discrete spatial domain of  $\mathcal{D}$ .

Notice that, the input segmented clinical bCT VOIs depict adipose compartments, from which it might be difficult to discern the individual ellipsoids. This means that the positions of the ellipsoid centers are *unobservable* from the ground truth data  $\mathcal{D}$ . This unobservability makes it difficult to propose an appropriate parametric model for the ellipsoid center point process. Also, multiple configurations of ellipsoids may be possible to approximate the adipose tissue in  $\mathcal{D}$ , making the inference problem ill-posed.

### III. EXISTING PARAMETER INFERENCE METHODS FOR MARKED POINT PROCESSES WITH UNOBSERVABLE POINT POSITIONS

Due to the data unobservability problem described in the previous section, direct application of common MPP parameter inference approaches such as the *likelihood*-based approaches [?] [?] [?] [?] is no longer possible, since they require the knowledge of the positions of the ellipsoid centers [?]. Several classical inference method used in stochastic geometry can potentially mitigate the issue of data unobservability.

The *minimum contrast estimation* (MCE) method can be configured such that the knowledge of point positions is no longer necessary.

Let  $\Theta$  denote the set of all parameters for  $\mathbf{Y}$ . Let  $\mathcal{C}(\mathcal{D}, \Theta)$  denote a contrast function depending on the ground truth  $\mathcal{D}$  and the parameters  $\Theta$ . The minimum contrast estimator is defined as [?]:

$$\hat{\Theta} = \operatorname{argmin}_{\Theta} \mathcal{C}(\mathcal{D}, \Theta). \quad (2)$$

Often,

$$\mathcal{C}(\mathcal{D}, \Theta) = \iint_{Y \times Y} \left( S(y_1, y_2; \Theta) - \hat{S}(y_1, y_2; \mathcal{D}) \right)^2 dy_1 dy_2, \quad (3)$$

where  $S(\cdot, \cdot; \Theta)$  is the analytical formula of one, or a weighted sum of several second-order summary statistics of  $\mathbf{Y}$ ; and  $\hat{S}(\cdot, \cdot; \mathcal{D})$  denotes the empirical counterpart of  $S(\cdot, \cdot; \Theta)$  measured from the ground truth  $\mathcal{D}$ . Popular choices of summary statistics are the two-point function [?] and the contact distribution function [?] etc.

The MCE method has limitations that make its application in our case difficult. The major limitation is the difficulty in the derivation of analytical summary statistics when the underlying model  $\mathbf{Y}$  deviates from the Poisson MPP model. Previous applications of the MCE almost always assumed  $\mathbf{Y}$  to be a Poisson MPP with disc or spherical marks [?] [?]. These assumptions seem to be too strong in our inference problem. When the parametric form of  $\mathbf{Y}$

becomes complicated, the derivation of summary statistics may involve some numerical integration technique and the minimization can also be non-trivial.

Another statistical estimation approach based on the *Takacs-Fiksel estimation* method [?] has recently been proposed for a particular class of MPP named the *Quermass model* [?]. The Takacs-Fiksel estimation method consists in choosing a number of test functions that are analytically or computationally accessible and can be empirically measured from ground truth data even with unobservable point positions. The parameter estimations is then carried out by minimizing an objective function defined by the analytical test functions and their empirical measurements. The method has been applied to Quermass model of 2D discs for binary images [?] and was proven to give more satisfactory result than previously proposed methods [?].

The Takacs-Fiksel estimation method also has limitations. The authors in [?] pointed out that, in order to avoid the identifiability problem, the number of test functions should be much greater than the number of model parameters. Considering the number of parameters in our texture model, it might be challenging to find enough test functions to apply the TFE method. Also, when the number of parameters is too large, the TFE method might yield non-satisfactory results due to strong statistical variability [?].

### IV. THE METHOD OF INFERENCE FROM RECONSTRUCTION

Recently, Thiedmann *et al.* proposed a novel inference method for parametric MPP models using a two-step approach that can effectively mitigate the challenges in our inference problem caused by data unobservability [?]. Inspired by their work, we hereby formally present this method and refer to it as the *inference from reconstruction* method.

The inference from reconstruction method consists of two steps:

- 1) *The reconstruction step* aims at recovering the unobserved points and marks from the observed data through stochastic random sampling.
- 2) *The inference step* is a parametric inference step where a marked point process models is proposed and fitted to the reconstructed points and marks.

This two-step mechanism provides two advantages that classical MCE method and the TFE method do not share. First, the recovered points and marks provide intuitions to determine which model should be used for the inference step. For example, once the points and marks are available, we can visualize and analyze their summary statistics to study statistical properties of the reconstructed points and marks. Second, the inference step using reconstructed points and marks becomes more straightforward since all point positions are observable. For instance, the reconstructed points can be fitted separately from the marks, using methods described in Section ??, and the marks

can be fitted later by separately analyzing their empirical statistics.

In the literature, limited studies have investigated the inference from reconstruction method for parameter estimation of stochastic geometric models. In [?], the authors first reconstructed a set of random Boolean discs from the binary Li-ion battery images using a stochastic disc sampling algorithm. Then a planar Matérn elliptical cluster point process was fitted to the recovered disc centers using the minimum contrast method with pair correlation function. The distribution of disc radii was analyzed separately. In [?], Dereudre *et al.* has applied the reconstruction method described in [?] in order to facilitate the empirical measurements of test functions from the input images during the TFE procedure for the Quermass disc model. To our knowledge, the method of inference from reconstruction has not yet been investigated for more complicated MPP models such as our case.

Due to the previously described advantages, we decided to apply the inference from reconstruction method to fit a parametric MPP model to the ground truth segmented bCT data. In the following section we describe in detail the methodology used for the reconstruction step and the inference step in our study.

#### A. Reconstruction step: approximating segmented bCT data using ellipsoids

Consider the case where the density function  $f_{\mathbf{Y}}$  of the underlying MPP model  $\mathbf{Y}$  has a Gibbsian form [?]. Let  $\mathbf{u} \in Y$  be a set of ellipsoids, referred to as a configuration, then we have:

$$f_{\mathbf{Y}}(\mathbf{u}) = \frac{1}{Z} \exp\left(-\frac{1}{T}U(\mathbf{u})\right). \quad (4)$$

Here the term  $U(\cdot)$  is called the *energy*. The parameter  $T \in \mathbb{R}^+$  is often referred to as the temperature in physics. The term  $Z = \int \exp(-U(\mathbf{u})) d\mathbf{u}$  is a normalization constant. The energy term is often decomposed into two parts [?]:

$$U(\mathbf{u}) = \mathcal{L}(\mathbf{u}, \mathcal{D}) + \mathcal{P}(\mathbf{u}), \quad (5)$$

where  $\mathcal{L}(\mathbf{u}, \mathcal{D})$  is a *data term* representing how well a configuration  $\mathbf{u}$  matches the observed dataset  $\mathcal{D}$ ; and  $\mathcal{P}(\cdot)$  is a *prior term* containing the a-priori information of the underlying MPP model  $\mathbf{Y}$ . Finding the best set of ellipsoids  $\mathbf{u}^*$  is equivalent to solving the following optimization problem:

$$\begin{aligned} \mathbf{u}^* &= \arg \max_{\mathbf{u}} f_{\mathbf{Y}}(\mathbf{u}) \\ &= \arg \min_{\mathbf{u}} U(\mathbf{u}, \mathcal{D}) \\ &= \arg \min_{\mathbf{u}} (\mathcal{L}(\mathbf{u}, \mathcal{D}) + \mathcal{P}(\mathbf{u})). \end{aligned} \quad (6)$$

We formulated  $\mathcal{L}(\mathbf{u}, \mathcal{D})$  and  $\mathcal{P}(\mathbf{u})$  as follows:

- The *data term*  $\mathcal{L}(\mathbf{u}, \mathcal{D})$  quantifies the approximation quality of the current configuration  $\mathbf{u}$  with respect to the input  $\mathcal{D}$ . It consists of two terms  $\mathcal{L}_1$  and  $\mathcal{L}_2$ . The first term  $\mathcal{L}_1$  measures the total approximation error of the current configuration  $\mathbf{u}$  given input  $\mathcal{D}$ .

For a given ellipsoid  $\mathcal{E} \in \mathbf{u}$ , its approximation error term  $d_{\mathcal{E}}(\mathcal{D})$  can be expressed as:

$$d_{\mathcal{E}}(\mathcal{D}) = \frac{|\{x \in \Omega | x \in \mathcal{E} \text{ and } \mathcal{D}(x) = 1\}|}{|\{x \in \Omega | x \in \mathcal{E}\}|}. \quad (7)$$

The term  $\mathcal{L}_1$  is then defined by summing the error terms of all ellipsoids. That is,

$$\mathcal{L}_1(\mathbf{u}, \mathcal{D}) = \sum_{\mathcal{E} \in \mathbf{u}} d_{\mathcal{E}}(\mathcal{D}). \quad (8)$$

The second term  $\mathcal{L}_2$  measures the proportion of the input  $\mathcal{D}$  that is not covered by the current configuration  $\mathbf{u}$ . That is,

$$\mathcal{L}_2(\mathbf{u}, \mathcal{D}) = 1 - \frac{|\{x \in \Omega | x \in \mathbf{u} \text{ and } \mathcal{D}(x) = 0\}|}{|\{x \in \Omega | \mathcal{D}(x) = 0\}|}. \quad (9)$$

The sum of  $\mathcal{L}_1$  and  $\mathcal{L}_2$  defines the final data term  $\mathcal{L}$ . That is,

$$\mathcal{L}(\mathbf{u}, \mathcal{D}) = \mathcal{L}_1(\mathbf{u}, \mathcal{D}) + \mathcal{L}_2(\mathbf{u}, \mathcal{D}). \quad (10)$$

- Regarding the *prior term*  $\mathcal{P}(\mathbf{u})$ , we prefer to obtain a model estimate without imposing too much a-priori information on the distribution of the ellipsoids. Hence, only a weak constraint on the overlap ratio between ellipsoids is used to formulate  $\mathcal{P}(\mathbf{u})$ . That is:

$$\mathcal{P}(\mathbf{u}) = \sum_{\mathcal{E} \in \mathbf{u}} q(\mathcal{E}, \mathbf{u} \setminus \mathcal{E}), \quad (11)$$

where

$$q(\mathcal{E}, \mathbf{u} \setminus \mathcal{E}) = \begin{cases} 0 & \text{if } \frac{|\{x \in \Omega | x \in \mathcal{E} \text{ and } x \in \mathbf{u} \setminus \mathcal{E}\}|}{|\{x \in \Omega | x \in \mathcal{E}\}|} \leq 0.95, \\ +\infty & \text{otherwise.} \end{cases} \quad (12)$$

This means that the only a-priori information of the model  $\mathbf{Y}$  is that there are no ellipsoids that can have more than 95% percent of its volume covered by other ellipsoids in the same configuration.

The optimization given by (6) finally becomes:

$$\begin{aligned} \mathbf{u}^* &= \arg \min_{\mathbf{u}} U(\mathbf{u}, \mathcal{D}) \\ &= \arg \min_{\mathbf{u}} \mathcal{L}_2(\mathbf{u}, \mathcal{D}) + \sum_{\mathcal{E} \in \mathbf{u}} (d_{\mathcal{E}}(\mathcal{D}) + q(\mathcal{E}, \mathbf{u} \setminus \mathcal{E})). \end{aligned} \quad (13)$$

The analytical solution of (13) is difficult to obtain and the Markov chain Monte Carlo sampling is often applied to find the optimum [?]. In the literature, the *reversible jump Markov chain Monte Carlo* (RJMCMC) sampling is the most commonly applied method for MPP models [?] [?] [?] [?] [?] [?] [?].

A typical RJMCMC procedure consists of iteratively simulating a Markov chain of configurations  $\{\mathbf{u}_t\}_{t \in \mathbb{N}}$  that converges to the target density  $f_{\mathbf{Y}}(\mathbf{u})$ . At each iteration  $t$ , a modification of the current configuration  $\mathbf{u}_t$  is proposed to create the next configuration  $\mathbf{u}_{t+1}$ . The term “jump” refers to the fact that the cardinality, *i.e.* the number of marked points of the current configuration might change during the modification. A modification in RJMCMC is performed according to a density function  $Q(\mathbf{u}_t, \mathbf{u}_{t+1})$ , referred to as a proposition kernel. The modifications

are local, in the sense that for each iteration only one or two marked points in the current configuration are modified. Typically,  $Q(\mathbf{u}, \cdot)$  is a combination of several sub-proposition kernels:

$$Q(\mathbf{u}, \cdot) = \sum_n p_n Q_n(\mathbf{u}, \cdot), \quad (14)$$

where  $p_n$  is the probability of the occurrence of the sub-proposition kernels  $Q_n(\cdot, \cdot)$ , such that  $\sum_n p_n \leq 1$  [?] [?]. Frequently investigated sub-proposition kernels include:

- The *Birth proposal*, in which a marked point is added to current configuration  $\mathbf{u}_t$ , according to a birth kernel denoted as  $Q_b(\mathbf{u}, \cdot)$ . That is,  $\mathbf{u}_{t+1} = \mathbf{u}_t \cup \{u\}$ , where  $u$  is drawn according to  $Q_b(\mathbf{u}, \cdot)$ .
- The *Death proposal*. This is the reverse process of the birth proposal, in which a marked point is chosen and deleted from current configuration  $\mathbf{u}$  according to a death kernel  $Q_d(\mathbf{u}, \cdot)$ . That is,  $\mathbf{u}_{t+1} = \mathbf{u}_t \setminus \{u\}$ , with  $u \in \mathbf{u}_t$  chosen according to  $Q_d(\mathbf{u}, \cdot)$ .  
The combination of birth and death proposals ensures that the Markov chain is able to switch between configurations with different cardinality.
- *Perturbation proposal*. This proposal consists of changing the parametrization of a marked point  $u$  in the current configuration  $\mathbf{u}$  according to a perturbation kernel  $Q_p(\mathbf{u}, \cdot)$ . There are various choices for the type of perturbation. Commonly applied choices include affine transformations of a mark [?], diffusion based on the Langevin equations [?], perturbation driven by observed data [?], or even switching to a different type of mark [?] [?].

In practice, the RJMCMC procedure might suffer from prohibitive rate of convergence, since each iteration brings only one or two marked points into play [?]. To mitigate this issue, a *multiple births and deaths* algorithm has recently been proposed by Descombes *et al.* [?], allowing for the births of multiple marked points at each iteration, offering a more effective sampling procedure. In our study, we adapted the multiple births and deaths algorithm design proposed in [?]. For each iteration, the original multiple births and deaths algorithm consisted of a birth step of multiple marked points and a death step that examines all marked points in current configuration. Additionally, to achieve a more effective exploration of each configuration, we proposed to add an extra perturbation step to the multiple births and deaths algorithm, named as the *shift* step.

To describe the shift step used in our adapted multiple births, deaths and shifts (MBDS) algorithm, we adopt the notion of *Legendre ellipsoid* of a convex body in classical mechanics [?]. Given a volume  $K \subset \mathbb{Z}^3$ , the Legendre ellipsoid  $\mathcal{L}(K)$  is the unique ellipsoid defined as [?]:

$$\mathcal{L}(K) = \{x \in K | x^T \Sigma^{-1} x \leq 1\}, \quad (15)$$

where

$$\Sigma = \frac{\sum_{x \in K} (x - \mu)(x - \mu)^T}{|K|}, \quad (16)$$

with  $\mu = \frac{1}{|K|} \sum_{x \in K} x$ . Notice that  $\mathcal{L}(K) = K$  if  $K$  is itself an ellipsoid.

In our proposed MBDS algorithm, the shift of an ellipsoid  $\mathcal{E}$  consists in replacing it by the Legendre ellipsoid computed from the part of the adipose tissue of the observed data  $\mathcal{D}$  inside  $\mathcal{E}$ . That is,

$$\mathcal{E} \rightarrow \mathcal{L}(K_{\mathcal{E}}(\mathcal{D})) \text{ with } K_{\mathcal{E}}(\mathcal{D}) = \{x \in \Omega | x \in \mathcal{E} \text{ and } \mathcal{D}(x) = 0\}. \quad (17)$$

The complete description of the proposed MBDS algorithm is given by Algorithm I.

The decrease of temperature by a factor  $\alpha$  in each iteration performs the simulated annealing [?] with geometric cooling schedule. Starting from a high temperature, the death probability of a marked point is relatively small. This means that the births and shifts are more favored than deaths in the beginning. This allows the Markov chain to broadly explore the solution space, and prevents it from getting stuck in local optima. As the temperature decreases, the death probability keeps increasing. The algorithm favors more deaths than births and shifts, since it assumes that the Markov chain is more concentrated on the global optimum as iterations advance.

The parameters for the MBDS algorithm are summarized in Table I. Values for  $T_0$ ,  $\lambda_0$  and  $\alpha$  were empirically determined such that the convergence of the MBDS algorithm was obtained in a reasonable number of iterations (Section V-A). We assumed that the proposal distribution  $f_{\theta} = \{f_{L_a}, f_{L_b}, f_{L_c}, f_{\delta\phi_x}, f_{\delta\phi_y}, f_{\delta\phi_z}\}$ , where  $f_{L_a}$ ,  $f_{L_b}$ ,  $f_{L_c}$ ,  $f_{\delta\phi_1}$ ,  $f_{\delta\phi_2}$  and  $f_{\delta\phi_3}$  are independent densities to sample the half lengths  $L_a$ ,  $L_b$ ,  $L_c$  and the tilt angles  $\delta\phi_x$ ,  $\delta\phi_y$ ,  $\delta\phi_z$ . We set these densities to the ones used in the empirical texture model for the BI-RADS breast density 2 type breasts (Section ??) because these previously validated values might provide a good starting-point for the MBDS algorithm and might accelerate the convergence of the algorithm.

### B. Inference step: fitting a marked point process model to reconstructed ellipsoids

Once a segmented bCT VOI is represented as a system of ellipsoids with known spatial positions and shape parameters, we can fit a parametric MPP model to the reconstructed ellipsoids using methods described in Section ???. To reduce the complexity of the inference step, we assume in the first instance that the marks of the MPP model is independent from the ground point process. This allows us to fit the center point process of the ellipsoids and their shape parameters separately.

To gain some intuition on the type of point process model  $\Phi_s$  to fit to the reconstructed ellipsoid centers, we first conducted statistical analysis to extract distributional information of the ellipsoid centers. In stochastic geometry, the analysis of summary statistics is the most commonly performed technique for this purpose [?]. In this study, we chose to analyze the *pair correlation function* (PCF), a second-order statistical characteristic that can help reveal comprehensive structural information of a point process.

**Algorithm:** Multiple births, deaths and shifts• **Initialization.**

Set the initial configuration  $\mathbf{u}_0 = \emptyset$ , the initial temperature  $T = T_0$ . Let  $\Phi$  be a Poisson point process with initial intensity parameter  $\lambda = \lambda_0$ . Let  $f_\theta$  be a multivariate proposal distribution used to sample  $(L_a, L_b, L_c, \delta\phi_1, \delta\phi_2, \delta\phi_3)$ , *i.e.* the marks.

• **Iterations**

Iterate the following steps in order, until convergence is reached.

– **Multiple births**

Generate a random configuration  $u_b$  with ellipsoid centers drawn from  $\Phi$  and ellipsoid parameters drawn from  $f_\theta$ . Update current configuration  $\mathbf{u}$ :

$$\mathbf{u} \rightarrow \mathbf{u} \cup u_b. \quad (18)$$

– **Computation of death probabilities**

For each ellipsoid  $\mathcal{E} \in \mathbf{u}$ , the death probability  $p_d$  is given by [?]:

$$p_d = \frac{r\lambda}{1+r\lambda}, \quad (19)$$

with  $r = \exp\left(\frac{U(\mathbf{u}) - U(\mathbf{u} \setminus \mathcal{E})}{T}\right)$ , where  $U(\cdot)$  is given in (13).

– **Deaths and shifts**

For each ellipsoid  $\mathcal{E} \in \mathbf{u}$ , draw a random variable  $v \sim \text{uniform}(0, 1)$ .

**if**  $v < p_d$ , perform a death operation:  $\mathbf{u} \rightarrow \mathbf{u} \setminus \mathcal{E}$   
**else**, shift  $\mathcal{E}$  to its Legendre ellipsoid:  $\mathcal{E} \rightarrow \mathcal{L}(\mathcal{K}_{\mathcal{E}(\mathcal{D})})$ , as described in (17).

– **Update parameters**

Decrease the Poisson intensity  $\lambda$  and the temperature  $T$ :

$$\lambda \rightarrow \lambda \cdot \alpha \text{ and } T \rightarrow T \cdot \alpha, \quad (20)$$

where  $\alpha \in (0, 1)$ .

• **Test of convergence**

For each iteration  $t$ , record its energy value and the energy values of its next nine successive iterations. This yields a set of ten energy values  $E_t = \{U_t, U_{t+1}, \dots, U_{t+9}\}$ . Then compute  $\max E_t$  and  $\min E_t$ . If for a predefined small real number  $\epsilon$ ,  $\max E_t - \min E_t \leq \epsilon$ , then the convergence is considered reached.

**Algorithm I****Definition IV.1. (Second order moment density, pair correlation function)** [?, p34]

The pair correlation function  $g(\cdot, \cdot)$  of a simple point process  $\Phi$  with intensity function  $\lambda(\cdot)$  is defined as:

$$g(x, y) = \frac{\rho^{(2)}(x, y)}{\lambda(x)\lambda(y)}. \quad (21)$$

Here  $\rho^{(2)}(\cdot, \cdot)$  is the second order moment density of  $\Phi$ ,

Parameter	Value
$T_0$	100
$\lambda_0$	0.005
$\alpha$	0.99
$\epsilon$	0.001
$f_{L_a}$	$\mathcal{N}(6.4, 1.5)$
$f_{L_b}, f_{L_c}$	$\mathcal{N}(2.5, 0.7)$
$f_{\delta\phi_x}$	$\mathcal{U}(-\frac{\pi}{2}, \frac{\pi}{2})$
$f_{\delta\phi_y}, f_{\delta\phi_z}$	$\mathcal{N}(0, \pi/12)$

TABLE I: Parameters of the MBDS algorithm to reconstruct a set of ellipsoids from each bCT VOI.

satisfying

$$\int_{B_1 \times B_2} \rho^{(2)}(x, y) dx dy = \sum_{\substack{x \neq y \\ x, y \in \Phi}} \mathbb{E}(\mathbf{1}(\{x, y\} \in B_1 \times B_2)), \quad (22)$$

for arbitrary bounded Borel sets  $B_1$  and  $B_2$ .

The PCF can be used to interpret important structural information of a point process. In particular,

- For all Poisson processes,  $g(x, y) = 1$ .
- If  $g(x, y) > 1$ , an *attraction* between points at locations  $x$  and  $y$  exists.
- If  $g(x, y) < 1$ , a *repulsion* between points at locations  $x$  and  $y$  exists.

For a stationary and isotropic point process, the PCF depends only on the relative distance between two spatial positions. That is,  $g(x, y) = g(r)$ , where  $r = \|x - y\|$  is referred to as the *interpoint distance*. In our study, we assumed that the centers of the reconstructed ellipsoids come from a stationary and isotropic point process. Following this assumption, the PCF of reconstructed ellipsoid centers from each segmented bCT VOI was estimated, using the PCF estimator described in [?, p232]. Analytically, the PCF estimator is expressed as:

$$\hat{g}(r; \Phi_s) = \sum_{\substack{x \neq y \\ x, y \in \Phi_s \cap W}} \frac{\mathbf{k}(\|x - y\| - r)}{4\pi r^2 \nu(W_x \cap W_y) \hat{\lambda}^2}, \quad (23)$$

where  $\Phi_s$  is the collection of all ellipsoid centers reconstructed from a dataset and  $\hat{\lambda}$  is an estimate of its intensity parameter, expressed as

$$\hat{\lambda} = \frac{|\Phi_s|}{\nu(W)}. \quad (24)$$

The function  $\mathbf{k}(\cdot)$  is a smoothing kernel. We use  $\nu(\cdot)$  to denote the volume measure and  $W$  is the observation window; *i.e.* a  $3.5 \text{ cm} \times 3.5 \text{ cm} \times 3.5 \text{ cm}$  cube in our case. Finally,  $W_x$  denotes the translation of  $W$  by  $x$ . The division by  $\nu(W_x \cap W_y)$  instead of by  $\nu(W)$  acts as an edge correction for points falling outside of the observation window  $W$  [?].

The estimation was performed using the `pcf3est` function implemented in the R software package `spatstat` [?] with its default setting. In this setting the *Epanechnikov*

*nikov* smoothing kernel [?] was used. Mathematically, the *Epanechnikov* kernel is defined as:

$$\mathbf{k}(s) = \begin{cases} \frac{3}{4\delta} (1 - \frac{s^2}{\delta^2}) & \text{if } -\delta \leq s \leq \delta, \\ 0 & \text{otherwise.} \end{cases} \quad (25)$$

It has a bandwidth parameter  $\delta$  to tune. In the default setting of `pcf3est`,  $\delta$  is set according to the rule-of-thumb:  $\delta = \frac{0.26}{\sqrt[3]{\lambda}}$  [?].

Once the empirical estimates of PCFs were obtained, we first checked if the Poisson property can or can not be rejected based on the PCF estimates. This check was performed using the envelope test described in [?].

In spatial point process theory, the envelope test is a commonly used statistical test procedure to determine whether empirically estimated summary statistics deviate from the same theoretical summary statistics of a null hypothesis point process model [?] [?]. The test procedure consists in comparing the empirical summary statistics with the envelope of the same summary statistics obtained from several simulations of the null hypothesis model.

Let  $\Phi$  be the null hypothesis model. Let  $S$  denote some second-order summary statistics. We assume that  $\Phi$  is stationary and isotropic, hence  $S$  is a function of the interpoint distance  $r$ . To construct the envelope of  $S$  using  $\Phi$  as the null hypothesis model, we first simulate  $N$  realizations of  $\Phi$ , denoted as the set  $\{\Phi_n\}_{n=1, \dots, N}$ . For a given realization  $\Phi_n$ , an empirical estimate of  $S$  is obtained, denoted as  $\hat{S}_n$ . Then we construct a point-wise envelope using the set of all empirical estimates  $\{\hat{S}_n\}_{n=1, \dots, N}$  as follows. At each interpoint distance  $r$ , we rank the values in  $\{\hat{S}_n(r)\}_{n=1, \dots, N}$  in ascending order. Then given a non-negative integer  $k$ , the envelope upper bound is assigned to the  $k^{\text{th}}$  highest value in  $\{\hat{S}_n(r)\}_{n=1, \dots, N}$ . Similarly, the envelope lower bound is assigned to the  $k^{\text{th}}$  lowest value in  $\{\hat{S}_n(r)\}_{n=1, \dots, N}$ .

Let  $\Phi_b$  be a spatial point pattern and let the null-hypothesis be that  $\Phi_b$  is drawn from the null hypothesis model  $\Phi$ . Let  $\hat{S}_b$  be the empirical estimate of  $S$  using  $\Phi_b$ . Then the envelope test is performed as follows. For a fixed interpoint distance value  $r$ , we reject the null-hypothesis at  $r$ , if  $\hat{S}_b(r)$  falls outside of the envelope at  $r$ . It has been proved that this procedure consists in a two-sided point-wise Monte Carlo test with significance level  $\frac{2k}{1+N}$  [?] [?].

We conducted the envelope test for each set of reconstructed ellipsoid centers. For a given set of reconstructed ellipsoid centers  $\Phi_s$ , the null hypothesis model was the homogeneous Poisson point process with intensity parameter equal to  $\hat{\lambda}$  estimated from  $\Phi_s$  using (24). We chose  $k = 5$  and  $N = 199$ , which yields a test significance level of 5%.

We will show in Section V-B that the analysis of the PCFs revealed a clustering interaction between reconstructed ellipsoid centers. To model the clustering interaction, we proposed to fit a three-dimensional *Matérn cluster process* [?] to the reconstructed ellipsoid centers. The 3D Matérn cluster process is a two-step process described as follows.

1) First, a set of “parent points”  $\{y_i\}_{i \in \mathcal{I}} \subset \mathbb{R}^3$  are

sampled from a homogeneous Poisson point process with intensity parameter  $\kappa$ . For each “parent point”  $y_i$  with  $i \in \mathcal{I}$ , a sphere with radius  $R$  centered at  $y_i$  is generated.

2) Then, inside each obtained sphere, a set of “children points” are sampled from another homogeneous Poisson point process with intensity parameter  $\lambda_0$ . A realization of the Matérn cluster process is obtained as the collection of all “children points”.

We can see that a Matérn cluster process model  $\Phi_{\mathcal{M}}$  is a stationary and isotropic point process completely determined by the three parameters:  $\kappa$ ,  $\lambda_0$ , and  $R$ . Moreover, theoretical formula for the PCF of a 3D Matérn cluster process is analytically accessible and is given by the following proposition [?, p376].

**Proposition IV.1. (Intensity and PCF of the Matérn cluster process)**

Let  $\Phi_{\mathcal{M}}$  be a Matérn cluster process with parameters  $\kappa, \lambda, R$ , then its intensity parameter  $\lambda$  is:

$$\lambda = \frac{4}{3} \pi R^3 \kappa \lambda_0. \quad (26)$$

Its pair correlation function  $g$  is:

$$g(r; \kappa, \lambda_0, R) = \begin{cases} 1 + \frac{3}{8\pi\kappa R^6} (R - \frac{r}{2})^2 (2R + \frac{r}{2}) & \text{if } 0 < r \leq 2R, \\ 1 & \text{if } r > 2R. \end{cases} \quad (27)$$

To fit a Matérn cluster process with parameters  $\kappa, \lambda, R$  to a set of reconstructed ellipsoid centers  $\Phi_s$ , we applied the minimum contrast estimation (MCE) method described in Section ???. For a given  $\Phi_s$ , the contrast function  $\mathcal{C}$  was computed based on the analytical and empirical PCF. That is,

$$\mathcal{C}(r; \kappa, \lambda_0, R, \Phi_s) = \sum_{r \in \mathcal{R}} (g(r; \kappa, \lambda_0, R) - \hat{g}(r; \Phi_s))^2, \quad (28)$$

where  $\hat{g}(r, \Phi_s)$  is given in (23) and  $g(r; \kappa, \lambda_0, R)$  is given in (27). Here  $\mathcal{R}$  denotes the set of interpoint distances considered by the MCE estimator. Additionally, (26) was used as an equality constraint. Let  $\Theta = (\kappa, \lambda_0, R)$ , for a given set of reconstructed ellipsoids  $\Phi_s$ , the MCE estimator  $\hat{\Theta}$  is formally expressed as:

$$\begin{aligned} \hat{\Theta} &= \arg \min_{\Theta} \sum_{r \in \mathcal{R}} (g(r; \kappa, \lambda_0, R) - \hat{g}(r; \Phi_s))^2, \\ \text{subjected to: } \hat{\lambda} &= \frac{4}{3} \pi R^3 \kappa \lambda_0. \end{aligned} \quad (29)$$

The optimization (29) was numerically solved using the function `fmincon` implemented in the `Matlab` software (version 2016b, The MathWorks Inc., Natick, Massachusetts, United States). The default setting of `fmincon` was used. In this setting, the *interior point* optimization method is applied, with the Hessian of the contrast function  $\mathcal{C}(\cdot)$  approximated using the *Broyden-Fletcher-Goldfarb-Shanno* algorithm. We set  $\mathcal{R}$  to be a set of values increasing from 0.2 mm to 30 mm with a step size of 0.2 mm.

All optimizations were run with an initial condition  $\kappa = 0.1$ ,  $\lambda_0 = 0.1$  and  $R = 1$ . The convergence was considered reached when the contrast function was non-decreasing in all feasible directions, within the a tolerance value of  $1 \times 10^{-6}$ . Since we were able to obtain fairly good fit for all input datasets (Section V-B), the impact of different configurations of the optimization function was considered out-of-scope in our study and was not investigated.

As discussed earlier, the mark distribution  $\mathbf{P}^\theta$  was assumed independent from the ellipsoid center point process  $\Phi_s$ . Based on this assumption, empirical statistics of each individual mark were examined separately from the ellipsoid centers.

Histograms of the half lengths  $L_a$ ,  $L_b$  and  $L_c$  of the reconstructed ellipsoids were obtained to visualize the empirical distributions of  $L_a$ ,  $L_b$  and  $L_c$ . For each half length of the reconstructed ellipsoids, the empirical mean  $\hat{\mu}$  and standard deviation  $\hat{\sigma}$  of were estimated. Next, two one-sample Kolmogorov-Smirnov tests [?] were performed for each axis.

- The first test has the objective to check if the distributions of the half lengths deviate from Gaussian distributions. It has the null-hypothesis that  $L_a$ ,  $L_b$  and  $L_c$  follow Gaussian distributions with mean and standard deviation equal to the corresponding empirical estimates. The  $p$ -value of each test was computed and denoted as  $p_1$ .
- The second test has the objective to check if the distributions of the half lengths deviate from the proposal distributions  $f_{L_a}$ ,  $f_{L_b}$ ,  $f_{L_c}$  specified in Table I respectively. This test has the null-hypothesis that  $L_a$ ,  $L_b$  and  $L_c$  follow the proposal distributions  $f_{L_a}$ ,  $f_{L_b}$  and  $f_{L_c}$ . The  $p$ -value of each test was computed and denoted as  $p_2$ .

In a similar fashion, the histograms of the tilts angles  $\delta\phi_x$ ,  $\delta\phi_y$  and  $\delta\phi_z$  of the reconstructed ellipsoids were also obtained. For each set of reconstructed ellipsoids, the empirical minimum and maximum of  $\delta\phi_x$ , as well as the empirical mean  $\hat{\mu}$  and standard deviation  $\hat{\sigma}$  of  $\delta\phi_y$  and  $\delta\phi_z$  were estimated. Similar to the axis lengths, two Kolmogorov-Smirnov tests were performed for each tilt angle.

- For  $\delta\phi_x$ , the first test has the objective to check if its distribution deviates from a uniform distribution. It has the null-hypothesis that  $\delta\phi_x$  follows a uniform distribution with minimum and maximum equal to the empirical estimates. For  $\delta\phi_y$  and  $\delta\phi_z$ , the first test has the objective to check if the two distributions deviate from Gaussian distributions. It has the null-hypothesis that  $\delta\phi_y$  and  $\delta\phi_z$  follow Gaussian distributions with mean and standard deviation equal to the empirical estimates. The  $p$ -value of each test was computed and denoted as  $p_1$ .
- The second test has the objective to check if the distributions of the tilt angles deviate from the proposal distributions  $f_{\delta\phi_x}$ ,  $f_{\delta\phi_y}$  and  $f_{\delta\phi_z}$  specified in Table I

respectively. It has the null-hypothesis that  $\delta\phi_x$ ,  $\delta\phi_y$  and  $\delta\phi_z$  follow the proposal distributions  $f_{\delta\phi_x}$ ,  $f_{\delta\phi_y}$  and  $f_{\delta\phi_z}$  respectively. The  $p$ -value of each test was computed and denoted as  $p_2$ .

Based on the empirical statistical analysis, independent distributions were proposed for each mark.

## V. RESULTS

A collection of 16 sets of segmented clinical bCT VOIs were selected for this study. The sizes of the selected bCT VOIs are  $3.5 \text{ cm} \times 3.5 \text{ cm} \times 3.5 \text{ cm}$ . The selected VOIs have BI-RADS density from category one to three and represent a subset of breasts with considerable variability in medium scale fibroglandular and inter-glandular adipose tissue. None of the VOIs contained a lesion. Table II summarizes the density and the size (in voxels) of the selected bCT VOIs, as well as and the size of the isotropic voxels of each VOI.

VOI	Density	Size in voxels	Voxel size
#1	57.2%	$99 \times 99 \times 99$	0.357 mm
#2	40.6%	$99 \times 99 \times 99$	0.354 mm
#3	25.1%	$94 \times 94 \times 94$	0.376 mm
#4	23.5%	$103 \times 103 \times 103$	0.341 mm
#5	17.4%	$103 \times 103 \times 103$	0.343 mm
#6	37.2%	$100 \times 100 \times 100$	0.351 mm
#7	32.9%	$112 \times 112 \times 112$	0.314 mm
#8	29.0%	$96 \times 96 \times 96$	0.366 mm
#9	25.7%	$97 \times 97 \times 97$	0.361 mm
#10	13.9%	$101 \times 101 \times 101$	0.349 mm
#11	14.5%	$128 \times 128 \times 128$	0.275 mm
#12	09.8%	$87 \times 87 \times 87$	0.405 mm
#13	27.1%	$107 \times 107 \times 107$	0.329 mm
#14	25.0%	$87 \times 87 \times 87$	0.405 mm
#15	20.5%	$124 \times 124 \times 124$	0.283 mm
#16	17.2%	$126 \times 126 \times 126$	0.279 mm

TABLE II: Summary of the glandular density, the size (in voxels) and the size of the isotropic voxels of the selected 16 sets of segmented clinical bCT VOIs.

In this section, we demonstrate the results of the inference from reconstruction method focusing on examples of four bCT VOIs (VOI #1, #3 #7, #11). We chose these four VOIs since their glandular densities cover BI-RADS breast density 1, BI-RADS breast density 2 and BI-RADS breast density 3 categories and they represent a fairly large variability of medium scale fibroglandular and inter-glandular adipose breast tissue. Further analyses were performed for all datasets listed in Table II and similar results were obtained.

### A. Reconstruction step

The result of the reconstruction step is demonstrated using the reconstructed VOIs shown in Figure 1. Reconstructed VOIs are binary volumes having the same spatial

and voxel size as their corresponding bCT VOIs. They were created by voxelizing the reconstructed ellipsoids from the MBDS algorithm and assigning value 0 to the ellipsoid interior. The coronal and sagittal slices of the original VOIs and the reconstructed VOIs at the same positions are shown in Figure 1. Moreover, projections images of the original VOIs and the reconstructed VOIs are also demonstrated. The projections were obtained by averaging the VOIs in the direction perpendicular to the transverse plane.

From Figure 1 we can see that the reconstructions by ellipsoids are not perfect. Despite this, the distribution and morphology of the medium scale fibroglandular and interglandular adipose tissue in reconstructed VOIs agree fairly well with the original segmented clinical bCT VOIs. Also, the medium scale texture variations in the projections of the original VOIs are preserved in the projections of the reconstructed VOIs. The result of the reconstruction step provides sufficiently good input for follow-up inference step which focuses only on the medium scale fibroglandular and interglandular tissue.

To demonstrate the convergence of the MBDS algorithm, Figure 2 shows the decrease of the energy with the increasing number of iterations for the four examples of bCT VOIs. From this figure we can see that the convergence was reached after about 7500 iterations for all the cases. Similar results were obtained for other investigated bCT VOIs.

### B. Inference step

We first demonstrate the analysis of empirical PCFs estimated from the reconstructed ellipsoid centers for all selected bCT VOIs using methodologies described in Section ??.

Our analysis shows that, among the 16 selected bCT VOIs, there are four cases where the Poisson null-hypothesis can not be rejected. These four cases were VOI #5, #12 #15 and #16. Figure 3 compares the empirical PCFs estimated from the reconstructed ellipsoid centers for these four bCT VOIs and the theoretical Poisson PCFs. The envelopes of the Poisson PCFs generated using the method described in Section ?? are also shown. Based on the envelope test described in Section ??, the Poisson null-hypothesis can not be rejected at any interpoint distance. Due to this finding, the VOI #5, #12 #15 and #16 were left out for the follow-up study since they represented a much smaller population among all bCT VOIs.

Figure 4 compares the empirical PCFs estimated from the reconstructed ellipsoid centers for the four bCT VOIs shown in Figure 1 and the theoretical Poisson PCFs. The envelopes of the Poisson PCFs generated using the method described in Section ?? are also shown. Figure 4 indicates that the empirical PCFs estimated from the reconstructed ellipsoid centers of the four VOIs exhibit a clustering effect. This can be seen if we look at the interpoint distance  $r = 3\text{mm}$  emphasized in Figure 4. The envelope test rejects the null-hypothesis for all demonstrated VOIs at

$r = 3\text{mm}$ . The same clustering effect was found for all other investigated bCT VOIs.

*Parameters of the 3D Matérn cluster process:* As discussed in Section ??, a 3D Matérn cluster process was fitted to each set of reconstructed ellipsoid centers using the MCE method. Table III lists the fitted Matérn cluster process parameters  $\hat{\kappa}$ ,  $\hat{\lambda}_0$  and  $\hat{R}$  for ellipsoid centers reconstructed from all bCT VOIs (excluding VOI #5, #12, #15 and #16).

Figure 5 compares the empirical PCFs estimated from the reconstructed ellipsoid centers for the four bCT VOIs shown in Figure 1 and the theoretical PCFs of the Matérn cluster processes fitted to the same VOIs. The PCF envelopes of the fitted Matérn cluster processes were also generated using the method described in Section ??, but with the fitted Matérn cluster process as the null hypothesis model. It can be seen that for all VOIs, the empirically estimated PCFs fall inside the envelopes at all interpoint distances. Based on this, we conclude that the fits are fairly good.

VOI	$\hat{\kappa}$	$\hat{\lambda}_0$	$\hat{R}$
# 1	4.237e-04	2.812e-02	4.221
# 3	3.245e-03	5.985e-03	5.988
# 7	2.876e-04	3.092e-02	5.827
# 11	3.405e-03	1.923e-02	3.853

TABLE III: Fitted Matérn cluster process parameters for the four bCT VOIs shown in Figure 1.

*The mark distribution:* Figure 6 shows the histograms of the half lengths  $L_a$ ,  $L_b$  and  $L_c$  of the reconstructed ellipsoids for the four bCT VOIs shown in Figure 1. The empirical mean  $\hat{\mu}$  and standard deviation  $\hat{\sigma}$ , as well as the  $p_1$  and  $p_2$  values of the Kolmogorov-Smirnov tests (described in Section ??) for each half length are shown under the histograms.

According to the  $p_1$  values,  $L_a$ ,  $L_b$  and  $L_c$  remain to be Gaussian distributed for all cases at significance level 5%. However, according to the  $p_2$  values the distributions of  $L_a$ ,  $L_b$  and  $L_c$  deviate significantly from the proposal distributions  $f_{L_a}$ ,  $f_{L_b}$  and  $f_{L_c}$  respectively, for all cases at the same significance level.

Figure 7 shows the histograms of the tilts angles  $\delta\phi_x$ ,  $\delta\phi_y$  and  $\delta\phi_z$  of the reconstructed ellipsoids for the four bCT VOIs shown in Figure 1. The empirical minimum and maximum for  $\delta\phi_x$ , the empirical mean  $\hat{\mu}$  and standard deviation  $\hat{\sigma}$  for  $\delta\phi_y$  and  $\delta\phi_z$ , as well as the  $p_1$  and  $p_2$  values of the Kolmogorov-Smirnov tests (described in Section ??) for each tilt angle are shown under the histograms.

According to the  $p_1$  and  $p_2$  values for  $\delta\phi_x$ , the distribution of  $\delta\phi_x$  does not deviate significantly from the uniform distribution  $\mathcal{U}(-\frac{\pi}{2}, \frac{\pi}{2})$  for all cases at significance level 5%. According to the  $p_1$  values for  $\delta\phi_y$ ,  $\delta\phi_y$  remains to be Gaussian distributed in three of the four cases at significance level 5%. However, according to  $p_2$  values for  $\delta\phi_y$ , the distribution of  $\delta\phi_y$  deviates significantly from



the proposal distribution  $f_{\delta\phi_x}$  in three of the four cases at significance level 5%. According to the  $p_1$  values for  $\delta\phi_z$ ,  $\delta\phi_z$  remains to be Gaussian distributed in two of the four cases at significance level 5%. However, according to the  $p_2$  values for  $\delta\phi_z$ , the distribution of  $\delta\phi_z$  deviates significantly from the proposal distribution  $f_{\delta\phi_x}$  for all cases at significance level 5%. Similar observations were obtained for all other investigated bCT VOIs.

Based on these analyses, we proposed to model the distribution  $\mathbf{P}^\theta$  of the marks  $\theta = (L_a, L_b, L_c, \delta\phi_x, \delta\phi_y, \delta\phi_z)$  as independent densities  $p_{L_a}, p_{L_b}, p_{L_c}, p_{\delta\phi_x}, p_{\delta\phi_y}$  and  $p_{\delta\phi_z}$  respectively. These densities are specified as follows.

The distribution of the half lengths of the ellipsoids, namely  $p_{L_a}, p_{L_b}$  and  $p_{L_c}$  were all modeled as Gaussian distributions. The mean and standard deviation of  $p_{L_a}, p_{L_b}$  and  $p_{L_c}$  were determined by the values empirically measured from the ellipsoids reconstructed from the clinical bCT VOIs. The mean and standard deviation values were specified in Figure 6.

The distribution of the tilt angles  $\delta\phi_x, p_{\delta\phi_x}$  was model as the uniform distribution  $\mathcal{U}(-\frac{\pi}{2}, \frac{\pi}{2})$ , as suggested by its empirical distribution demonstrated in the previous section.

The distributions  $p_{\delta\phi_y}$  and  $p_{\delta\phi_z}$  were modeled as Gaussian distributions. Despite the fact that in some of the cases, the Gaussian hypothesis was rejected by the Kolmogorov-Smirnov tests, as mentioned in the previous section, in other majority of the cases the Gaussian hypothesis could not be rejected. Visual inspection of the histograms of  $p_{\delta\phi_y}$  and  $p_{\delta\phi_z}$  also suggests that the Gaussian distribution might still be a fairly reasonable choice. Similar to the half lengths, the mean and standard deviation of  $p_{\delta\phi_y}$  and  $p_{\delta\phi_z}$  are determined by the empirical estimates.

We finally obtained twelve new sets of medium scale parameters for the 3D solid breast texture model from the twelve input segmented bCT VOIs. Table IV lists the fitted medium scale parameters for the four bCT VOIs shown in Figure 1. Parameters fitted using the other eight bCT VOIs can be found in Appendix ??.

## VI. VALIDATION OF INFERRED MEDIUM SCALE TEXTURE MODEL PARAMETERS

### A. Visual validation

As a preliminary validation of the fitted medium scale texture model parameters, a simulation experiment in analogy to Section ?? was conducted.

Four texture volumes were simulated using the four sets of medium scale parameters listed in Table IV. The small scale textures in these volumes were also simulated using parameters listed in Table ??. The nipple position and the voxel size for each volume were set to be the same as in the corresponding ground truth bCT VOI. Mammograms and DBT projection images were simulated by virtually projecting the texture volumes using the previously described breast x-ray imaging simulator [?], with the same adjustment as described in Section ??.

VOI	$\Phi_s$ (Matérn cluster process)	$L_a, L_b, L_c$ (in mm)	$\delta\phi_x, \delta\phi_y, \delta\phi_z$ (in radian)
#1	$\kappa =$	$f_{L_a} =$	$p_{\delta\phi_x} =$
	$4.237e-04,$	$\mathcal{N}(5.48, 1.34),$	$\mathcal{U}(-\frac{\pi}{2}, \frac{\pi}{2}),$
	$\lambda_0 =$	$p_{L_b} =$	$p_{\delta\phi_y} =$
	$2.812e-02,$	$\mathcal{N}(2.72, 0.55),$	$\mathcal{N}(-0.05, 0.35),$
#3	$R = 4.221$	$p_{L_c} =$	$p_{\delta\phi_z} =$
		$\mathcal{N}(1.90, 0.48)$	$\mathcal{N}(-0.04, 0.53)$
	$\kappa =$	$p_{L_a} =$	$p_{\delta\phi_x} =$
	$3.245e-03,$	$\mathcal{N}(6.21, 1.41),$	$\mathcal{U}(-\frac{\pi}{2}, \frac{\pi}{2}),$
#7	$\lambda_0 =$	$p_{L_b} =$	$p_{\delta\phi_y} =$
	$5.985e-03,$	$\mathcal{N}(2.77, 0.58),$	$\mathcal{N}(-0.09, 0.4),$
	$R = 5.988$	$p_{L_c} =$	$p_{\delta\phi_z} =$
		$\mathcal{N}(2.10, 0.57)$	$\mathcal{N}(0, 0.26)$
#11	$\kappa =$	$p_{L_a} =$	$p_{\delta\phi_x} =$
	$2.876e-04,$	$\mathcal{N}(5.88, 1.44),$	$\mathcal{U}(-\frac{\pi}{2}, \frac{\pi}{2}),$
	$\lambda_0 =$	$p_{L_b} =$	$p_{\delta\phi_y} =$
	$3.092e-02,$	$\mathcal{N}(2.75, 0.56),$	$\mathcal{N}(-0.15, 0.38),$
#11	$R = 5.827$	$p_{L_c} =$	$p_{\delta\phi_z} =$
		$\mathcal{N}(2.03, 0.52)$	$\mathcal{N}(0.01, 0.5)$
	$\kappa =$	$p_{L_a} =$	$p_{\delta\phi_x} =$
	$3.405e-03,$	$\mathcal{N}(6.06, 1.39),$	$\mathcal{U}(-\frac{\pi}{2}, \frac{\pi}{2}),$
#11	$\lambda_0 =$	$p_{L_b} =$	$p_{\delta\phi_y} =$
	$1.923e-02,$	$\mathcal{N}(2.79, 0.56),$	$\mathcal{N}(-0.28, 0.47),$
	$R = 3.853$	$p_{L_c} =$	$p_{\delta\phi_z} =$
		$\mathcal{N}(2.10, 0.54)$	$\mathcal{N}(-0.01, 0.43)$

TABLE IV: Medium scale parameters for the 3D stochastic breast texture model fitted from the four bCT VOIs shown in Figure 1.

Mechanical breast texture deformation to mimic breast compression was not modeled for neither mammography and DBT simulation acquisitions. Projection images were processed by the ASiR-DBT 3D reconstruction algorithm (version 1.3.4, GE Healthcare, Buc, France) to obtain DBT reconstructed slices with 1 mm slice thickness.

Figure 8 shows examples of  $3.5\text{ cm} \times 3.5\text{ cm}$  slices through volumes simulated from the 3D breast texture model with the four sets of medium scale parameters listed in Table IV, as well as mammographic projections and DBT reconstructed slices simulated from these volumes. Images simulated with the other eight sets of parameters can be found in Appendix ??.

Visual inspection of the simulated images indicates high visual realism compared with the images simulated from segmented clinical bCT VOIs, shown in Figure ??. Also, compared with images simulated using the prototype implementation shown in Figure ??, the new model parameters are capable of simulating mammographic projections and and DBT reconstructed slices with a larger morphological variability. These observations indicate an improvement of the model's realism and morphological

variability compared with the prototype implementation with empirical parameters proposed in the previous chapter.

### B. Statistical validation

Computation of  $\beta$  values.

## VII. CONCLUSION AND DISCUSSION

In this chapter, we applied a novel methodology based on inference from reconstruction to automatically and objectively infer the medium scale 3D breast texture model parameters from  $3.5\text{ cm} \times 3.5\text{ cm} \times 3.5\text{ cm}$  volumes of interest (VOI) of segmented clinical breast computerized tomography (bCT) reconstructed datasets.

A multiple births, deaths and shifts (MBDS) algorithm was employed to first reconstruct a set of random ellipsoids from each ground truth bCT VOI. Visual inspection of the volumes recreated by voxelizing the reconstructed ellipsoids shows a fairly good approximation of the medium scale breast tissue in the original bCT VOIs. A Matérn cluster process was then fitted to the reconstructed ellipsoid centers using the minimum contrast method based on the pair correlation functions (PCF). This introduces a clustering interaction between ellipsoids to the previous prototype model. Statistical diagnostic analysis using the PCF suggested a fairly good fit of the reconstructed ellipsoid centers to the proposed Matérn cluster process. Distributions of the ellipsoid half lengths and orientations were finally estimated from their empirical distributions. Twelve sets of new medium scale model parameters were obtained. Preliminary evaluation of the 2D and 3D breast images simulated from 3D texture volumes generated using new parameters shows fairly high visual realism. The breast tissue variability in new simulated images is larger than the images simulated using previously proposed prototype implementation with empirical parameters.

The proposed method has several limitations. First, the impact of the reconstruction step on the estimated parameters in the inference step was not investigated. To address this, one possible approach is to study how the inference result deviates from a ground truth model when the latter is a known Poisson marked point process. Second, to reduce the optimization complexity in the inference step, the distribution of ellipsoid half lengths were estimated independently from the ellipsoid centers. This may be a simplification compared with the distribution of inter-glandular adipose compartments in real breasts. The correlation between the the half lengths and the centers of the ellipsoids could be further investigated by studying the mark correlation function of the reconstructed ellipsoids. The statistical properties of simulated 2D and 3D breast images using inferred medium scale model parameters were not studied. This should be addressed next as a further validation of the new models. Also, a formal observer psycho-physical experiment should be performed to validate the visual realism of images simulated using the fitted medium scale model parameters.

## ACKNOWLEDGMENT

This research is partially funded by the French national association for research and technology (ANRT) under the CIFRE grant n°2013/1052. The authors would like to thank Prof. John Boone for kindly providing the clinical bCT data sets.

## REFERENCES



**Michael Shell** Biography text here.

**John Doe** Biography text here.

**Jane Doe** Biography text here.

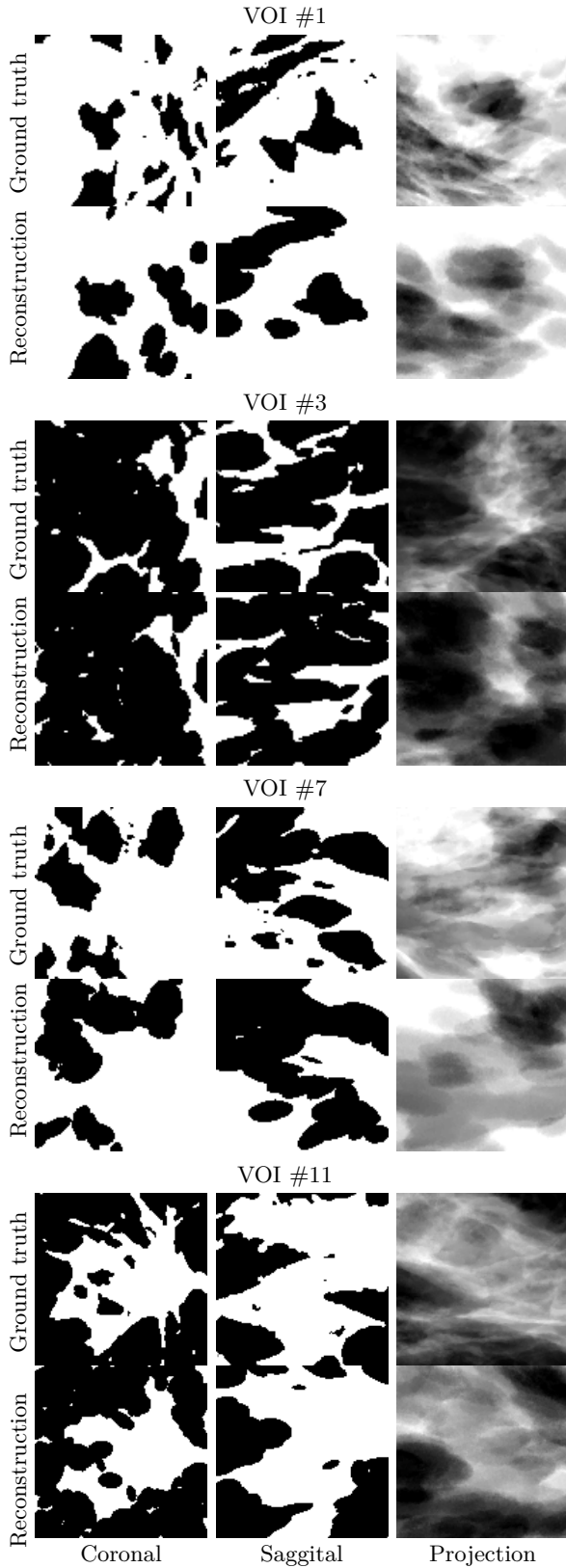


Fig. 1: From left to right, the three columns on the left shows: coronal slices through four segmented clinical bCT VOIs, sagittal slices through the same bCT VOIs and projections of the same bCT VOIs. From left to right, the three columns on the right shows: coronal slices through the reconstructed VOIs, sagittal slices through the reconstructed VOIs and projections of the reconstructed VOIs. The sizes of the VOIs are  $3.5 \text{ cm} \times 3.5 \text{ cm} \times 3.5 \text{ cm}$ . Reconstructed VOIs are binary volumes with the same size and resolution as their corresponding segmented clinical bCT VOIs. They were created by revealing the reconstructed

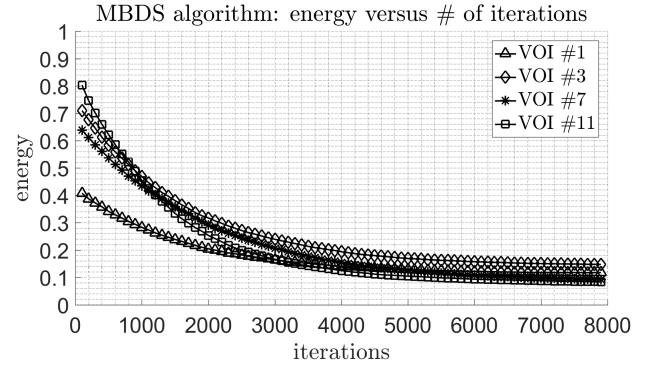


Fig. 2: Illustration of the energy defined in (5) as a function of the number of iterations in the MBDS algorithm. The illustration considers the four examples of segmented clinical bCT VOIs shown in Figure 1. The convergence of the MBDS algorithm was reached after about 7500 iterations for all the cases.

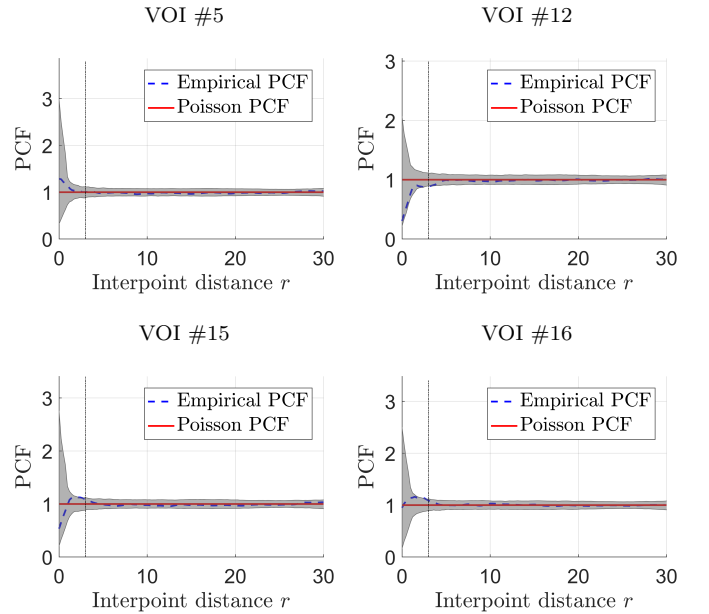


Fig. 3: Comparison of the empirical PCFs estimated from the reconstructed ellipsoid centers for four bCT VOIs (#5, #12 #15 and #16) and the theoretical Poisson PCFs. Dashed lines are the empirical PCFs estimated from the reconstructed ellipsoid centers. Solid lines are theoretical Poisson PCFs. Gray surfaces are the envelopes of the Poisson PCFs generated using the method described in Section ?? . Based on the envelope test described in Section ?? , the Poisson null-hypothesis can not be rejected at any interpoint distance.

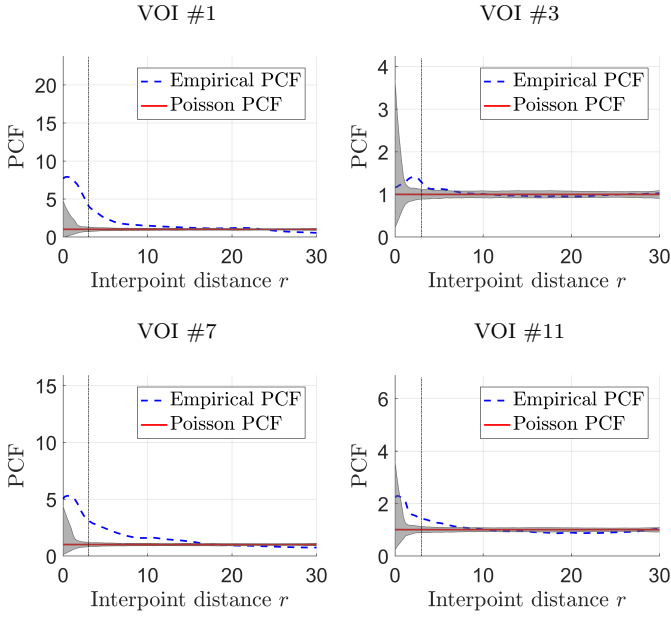


Fig. 4: Comparison of the empirical PCFs estimated from the reconstructed ellipsoid centers for the four bCT VOIs shown in Figure 1 and the theoretical Poisson PCFs. Dashed lines are the empirical PCFs estimated from the reconstructed ellipsoid centers. Solid lines are theoretical PCFs of the Poisson point processes. Gray surfaces are the envelopes of the Poisson PCFs generated using the method described in Section ???. The envelope test rejects the Poisson null-hypothesis for all four VOIs at interpoint distance  $r = 3$  mm.

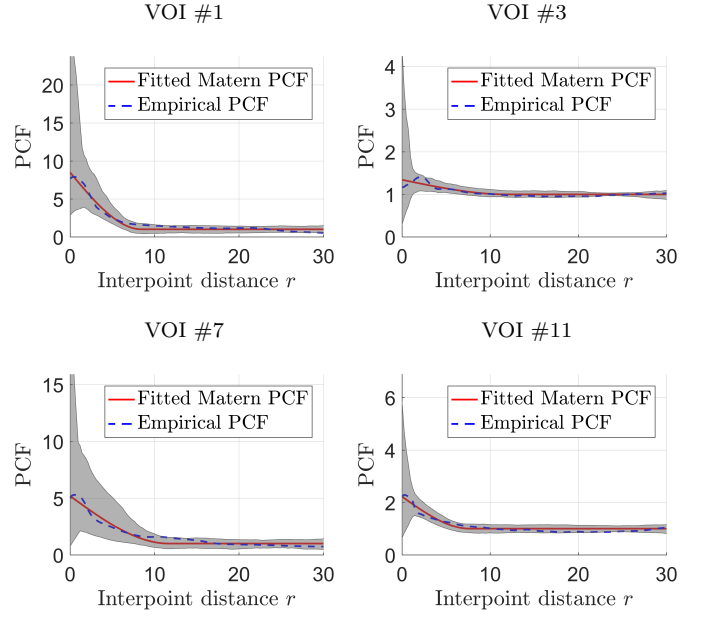


Fig. 5: Comparison of the empirical PCFs estimated from the reconstructed ellipsoid centers for the four bCT VOIs shown in Figure 1 and the theoretical PCFs of the Matérn cluster processes fitted to the same VOIs. Dashed lines are the empirical PCFs estimated from the reconstructed ellipsoid centers of the four VOIs. Solid lines are theoretical PCFs of the Matérn cluster processes fitted to the four VOIs. Gray surfaces are the envelopes of the PCFs of the fitted Matérn cluster processes generated using the method described in Section ???. The empirical PCFs fall inside the envelopes at all interpoint distances.

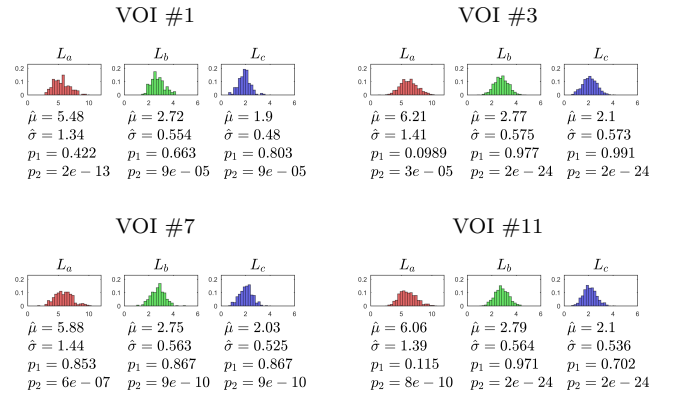


Fig. 6: Histograms of the half lengths  $L_a$ ,  $L_b$  and  $L_c$  of reconstructed ellipsoids for the four bCT VOIs shown in Figure 1. For each half length,  $\hat{\mu}$  and  $\hat{\sigma}$  refer respectively to their empirical mean and standard deviation. For each half length,  $p_1$  and  $p_2$  refer to the  $p$ -values of the two Kolmogorov-Smirnov tests described in Section ??.

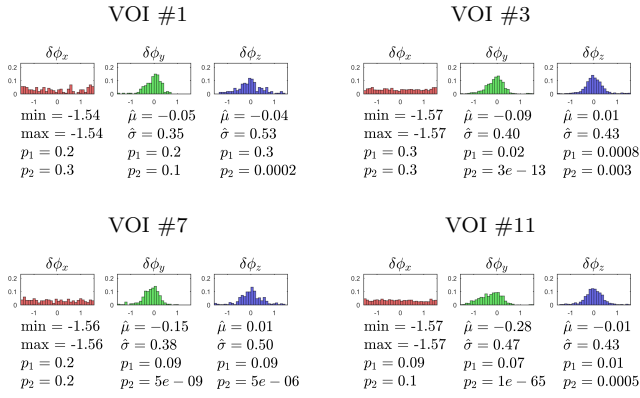


Fig. 7: Histograms of the tilt angles  $\delta\phi_x$ ,  $\delta\phi_y$  and  $\delta\phi_z$  of reconstructed ellipsoids from the four bCT VOIs shown in Figure 1. For  $\delta\phi_x$ , min and max refer respectively to its empirical minimum and maximum. For  $\delta\phi_y$  and  $\delta\phi_z$ ,  $\hat{\mu}$  and  $\hat{\sigma}$  refer respectively to their empirical mean and standard deviation. For each tilt angle,  $p_1$  and  $p_2$  refer to the  $p$ -values of the two Kolmogorov-Smirnov tests described in Section ??.

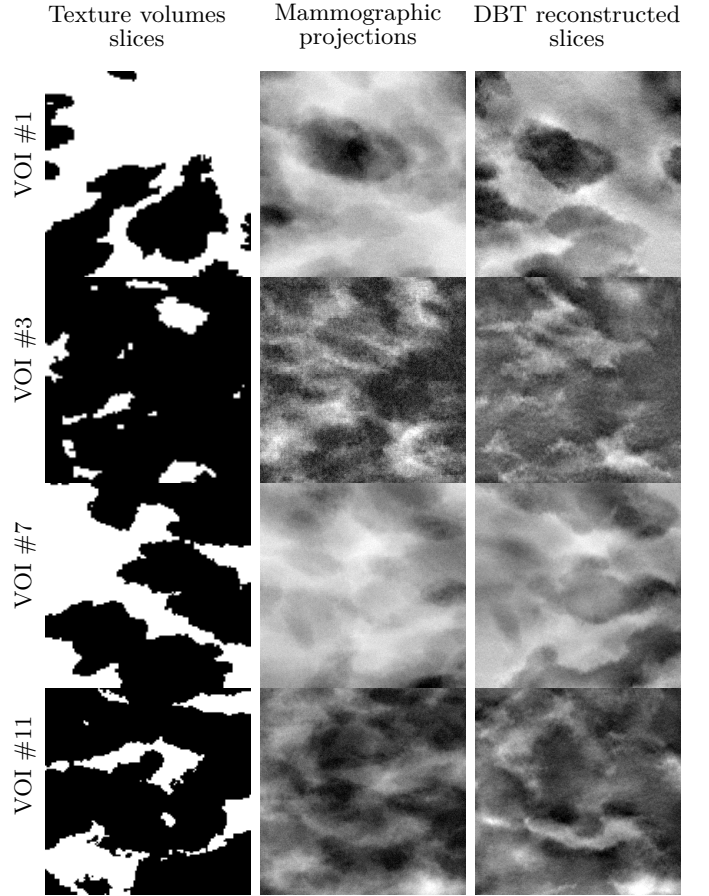


Fig. 8: The first column shows slices through volumes simulated from the 3D breast texture model with the four sets of parameters listed in Table IV. The second column shows mammographic projections simulated from the simulated texture volumes. The third column shows DBT reconstructed slices simulated from the simulated texture volumes. The sizes of the images are 3.5 cm  $\times$  3.5 cm.